



LABORATOIRE DE PHYSIQUE DE CLERMONT AUVERGNE
ATLAS TEAM

MASTER 2 INTERNSHIP

**Study of Long-Lived Particles in
ATLAS**

Submitted by:
LECOMTE Samuel

Under the guidance of:
CORPÈ Louie

Internship from February, 10 2025 to July, 11 2025

Contents

Introduction	1
1 Theoretical framework	2
1.1 The Standard Model	2
1.2 Long-Lived Particles	2
1.3 The Hidden Abelian Higgs Model	3
2 The ATLAS experiment	4
2.1 The LHC	4
2.2 The ATLAS detector	4
2.2.1 Subsystems	5
2.2.2 Trigger system and Event selection	6
2.3 Planned ATLAS Upgrades	6
2.3.1 High Granularity Timing Detector (HGTD)	6
2.3.2 Inner Tracker (ITk)	7
2.4 Observing Long-Lived Particles with ATLAS	7
3 Monte Carlo Event Generation	8
3.1 Overview and objectives	8
3.2 Monte Carlo algorithm	8
3.3 Rivet framework	9
3.4 Event generation with MG5	10
3.5 Parton shower and hadronization with PYTHIA 8	11
4 Preliminary Studies of Long-Lived Particle Kinematics	13
4.1 Description of the simulated LLP scenarios	13
4.2 Observables and kinematic distributions	15
4.2.1 Jet mass and transverse momentum distributions	15
4.2.2 Pseudorapidity distribution and detector acceptance	18
4.2.3 Role of cuts in improving signal detection	19
Conclusion	20
Bibliography	21
Appendices	A

Introduction

During the final year of my master's degree, I completed a four-month internship within the ATLAS team at the Clermont Physics Laboratory, under the supervision of Louie Corpe. The goal of this internship was to study the production mechanisms of long-lived particles, which are currently a promising target for probing physics beyond the Standard Model. The work carried out contributes to ongoing efforts that could eventually lead to the development of dedicated LLP searches.

My work focused on learning how to generate Monte Carlo collision events and applying these techniques to study LLP-related processes. This included implementing custom analysis routines and evaluating observables relevant to LLP signatures within the ATLAS detector and its future upgrades.

Chapters 1 and 2 provide the theoretical and experimental context necessary for this study. Chapter 3 presents the event generation framework and simulation tools used throughout the project. Finally, Chapter 4 describes preliminary applications of these methods to generate and analyse LLP events, with a focus on kinematic distributions and detector-level considerations.

Keywords:

ATLAS detector - LLPs - Displaced vertices - BSM physics

Chapter 1

Theoretical framework

1.1 The Standard Model

The Standard Model (SM) is currently the best theoretical framework we have to describe the fundamental particles and forces in nature. It successfully explains the electromagnetic, weak, and strong interactions between particles, providing a comprehensive understanding of the building blocks of matter.

The SM consists of two main families of particles: fermions and bosons. Fermions include particles such as quarks and leptons that make up matter. Quarks combine to form hadrons, which include mesons and baryons like protons and neutrons. Leptons, such as the electron and neutrinos, are fundamental particles that do not participate in the strong interaction. On the other hand, bosons are responsible for mediating the fundamental interactions. The photon mediates electromagnetism, the W and Z bosons the weak force, and the gluon the strong force. Discovered in 2012 [1], the Higgs boson plays an important role in the SM as it gives the mass of the particles through the Higgs field. Despite its successes, the SM has some limitations: it does not account for gravity, dark matter, and fails to explain the imbalance between matter and antimatter in the universe. These unresolved issues may suggest that the SM is part of a larger theory, and the search for new physics beyond the SM remains a key point in physics.

1.2 Long-Lived Particles

Long-Lived Particles are particles with lifetimes long enough to travel significant distances before decaying. Unlike most particles in the Standard Model, which decay almost immediately near the collision point, LLPs can decay far from the primary vertex, often leaving displaced vertices or isolated energy deposits in detectors. Their delayed decay is a key signature that makes them excellent probes for physics beyond the Standard Model (BSM), but this unique characteristic also complicates their detection, as the LHC reconstruction algorithms were not designed to account for this feature.

From a theoretical point of view, the lifetime τ of a particle is related to its total decay width Γ by the simple inverse relation:

$$\tau = \frac{\hbar}{\Gamma}$$

The decay width Γ can be expressed more precisely using the following general formula:

$$\Gamma = \int \frac{1}{2m_1} \left(\prod_{k=1}^n \frac{d^3 p'_k}{(2\pi)^3 2E'_k} \right) (2\pi)^4 \delta^{(4)} \left(p_1 - \sum_{k=1}^n p'_k \right) |\mathcal{M}_{fi}|^2$$

This expression comes from quantum field theory and corresponds to the integral over phase space of the final-state particles. A small decay width Γ , and thus a long lifetime, can result from two main mechanisms: either a suppressed matrix element $|\mathcal{M}_{fi}|^2$, typically due to weak couplings (meaning the particle interacts very rarely), or from a restricted phase space, as in decays with nearly equal initial and final masses. In other words, weak interactions imply fewer decay opportunities, leading naturally to longer-lived particles. Both situations frequently arise in SM and BSM models, potentially leading to LLPs.

1.3 The Hidden Abelian Higgs Model

Several theoretical frameworks have been proposed to describe the phenomenology of LLPs, including supersymmetry, hidden sector models, and Higgs or gauge portal scenarios. To facilitate reinterpretation and experimental coverage, simplified models have been developed, each characterized by distinct production and decay modes. These models help isolate key phenomenological features such as displaced vertices or non-standard track signatures. Among the available options, we chose to use the Hidden Abelian Higgs Model (HAHM) [2], which stands out for its simplicity and flexibility. It introduces a new hidden $U(1)$ gauge symmetry, associated with a neutral gauge boson Z' , and a scalar Higgs-like field ϕ_H , singlet under the SM, which mixes with the standard Higgs. This mixing enables communication between the SM and this hidden sector, where LLPs are produced. The mass eigenstates include a heavy scalar H that can decay into long-lived particles.

It is worth noting that several variations of the HAHM exist. Some versions contain two scalar particles, s_1 and s_2 , while others involve a single hidden scalar h_2 . For this study, we initially used a version of the HAHM developed at LPCA [3], designed specifically to simulate asymmetric decays of LLPs, in which the Higgs boson decays into two long-lived particles with different masses, lifetimes, or decay channels. However, this custom model quickly showed limitations, as it did not contain all the elementary particles required for our analysis. Consequently, we had to switch to a more complete implementation of the model to ensure accurate coverage of the final states under consideration. In this work, the HAHM primarily serves as a theoretical framework for tuning parameters such as the LLP mass and lifetime. Other components of the model, including the Z' boson or specific coupling values, are omitted as they would unnecessarily complicate the analysis.

Chapter 2

The ATLAS experiment

2.1 The LHC

The Large Hadron Collider (LHC) is the world's most powerful particle accelerator, located at CERN on the Franco-Swiss border. It consists of a 27-kilometer circular ring buried approximately 100 meters underground. This depth provides natural shielding from cosmic rays and radiation, allowing for precise measurements of particle interactions. The LHC is designed to accelerate and collide beams of protons (or heavy ions) at extremely high energies. The Center-of-Mass (CM) energy \sqrt{s} of the proton-proton collisions has increased with each run: 7-8 TeV in Run 1 (2010–2012), 13 TeV in Run 2 (2015–2018), and 13.6 TeV in Run 3 (2022–2026). Future runs at the High-Luminosity LHC (HL-LHC), expected to begin around 2030, aim to maintain $\sqrt{s} = 14$ TeV while significantly increasing the integrated luminosity.

The LHC conducts proton-proton (pp) collisions as well as heavy ion collisions (like Pb-Pb). These high-energy collisions allow scientists to try and better understand our universe by recreating conditions similar to those just after the Big Bang. The four major experiments at the LHC are ATLAS, CMS, ALICE, and LHCb. CMS and ATLAS are general-purpose experiments that search for new physics, such as the Higgs boson. ALICE focuses on studying the quark-gluon plasma, a state of matter thought to have existed just after the Big Bang. LHCb specializes in the study of the rare decays of particles containing b-quarks, helping to explore the matter-antimatter asymmetry.

In this report, we will focus on ATLAS, which will be discussed in detail in the following sections, as it is the experiment on which our study of Long-Lived Particles is based.

2.2 The ATLAS detector

The ATLAS (A Toroidal LHC ApparatuS) detector is one of the two general-purpose experiments at the LHC, designed to explore a wide range of physics phenomena, including the search for new particles. Figure 2.1 shows a complete view of the ATLAS detector, with its main components represented. The ATLAS detector is built around a cylindrical geometry centered on the interaction point, using a right-handed coordinate system. The origin is located at the nominal interaction point, with the z -axis along the beam pipe, the x -axis pointing from the interaction point to the center of the LHC ring, and the y -axis pointing upwards. The detector covers almost the entire solid angle around the collision point, corresponding to 4π in spherical coordinates.

An important variable used throughout detector physics is the pseudorapidity η , which is

defined in terms of the polar angle θ as:

$$\eta = -\ln \tan\left(\frac{\theta}{2}\right)$$

Pseudorapidity is preferred over the polar angle in collider physics due to its Lorentz invariance under boosts along the beam axis. It provides a convenient measure of how close a particle is to the beam direction: low values of $|\eta|$ correspond to particles emitted perpendicularly to the beam axis (central region), while high values of $|\eta|$ correspond to particles emitted at small angles with respect to the beam axis, i.e., in the forward region.

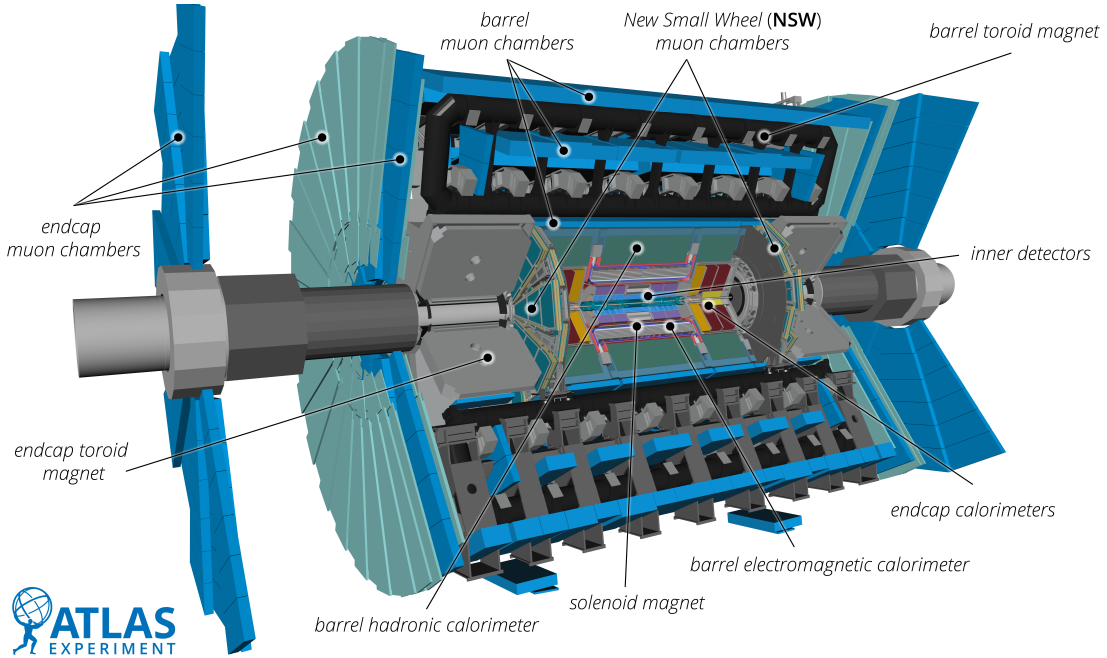


Figure 2.1: View of the ATLAS detector [4].

2.2.1 Subsystems

The detector is a large, complex instrument consisting of several subsystems, each with a specialized function to reconstruct and measure the properties of particles produced in LHC collisions. The subsystems include the inner detector, calorimeters, the magnet system, and the muon system.

The Inner Detector (ID) is the first subsystem that charged particles pass through after the collision. It covers the pseudorapidity range $|\eta| < 2.5$ and operates within a 2 T axial magnetic field. It consists of three main components: the Pixel Detector, the Semiconductor Tracker (SCT), and the Transition Radiation Tracker (TRT). The Pixel Detector provides high resolution tracking near the collision point, the SCT offers precise measurements at medium distances, and the TRT tracks longer-distance particles, particularly providing identification for electrons and hadrons. These detectors are crucial for reconstructing the trajectories and vertex positions of charged particles.

The Calorimeter System is designed to measure the energy of particles and covers up to $|\eta| < 4.9$. It is divided into two main parts: an Electromagnetic calorimeter (Ecal) and a Hadronic calorimeter (Hcal). The Electromagnetic Calorimeter, based on Liquid Argon (LAr) technology, measures electromagnetic energy from particles like electrons and photons with

high precision. It covers the pseudorapidity range $|\eta| < 3.2$ and consists of a barrel and two endcaps. The Hadronic Calorimeter, responsible for measuring hadronic energy, uses scintillator tiles in the barrel region ($|\eta| < 1.7$) and copper/LAr technology in the Hadronic Endcap Calorimeters, extending coverage up to $|\eta| < 3.2$. Finally, the Forward Calorimeters (FCal), based on copper/tungsten-LAr technology, increase the coverage to $|\eta| < 4.9$.

The Magnet System consists of a central solenoid around the ID and large air-core toroidal magnets surrounding the calorimeters and muon chambers. The full system provides a bending power of 2 to 4T across the detector, curving the trajectories of charged particles, allowing for precise momentum measurements.

The Muon System covers $|\eta| < 2.7$ and is designed to detect muons, which are commonly produced in particle decays and often appear in high-energy collisions. It is the outermost subsystem of the ATLAS detector and consists of Monitored Drift Tubes (MDTs) for precision tracking, and Resistive Plate Chambers (RPCs) and Thin Gap Chambers (TGCs) for triggering.

2.2.2 Trigger system and Event selection

The ATLAS trigger system is essential for selecting interesting events from the large volume of data produced by LHC collisions. It operates in two stages: Level 1 (L1) and High-Level Trigger (HLT). The L1 is a hardware-based system that quickly reduces the event rate by using data from the calorimeters and the muon system, bringing it down from 40 MHz to around 100 kHz. The HLT, a software-based system, performs a more detailed analysis, refining event selection by reconstructing particle trajectories, which reduces the rate further to around 1 kHz.

2.3 Planned ATLAS Upgrades

To maintain excellent performance under the conditions expected at the High-Luminosity LHC (HL-LHC), the ATLAS detector will undergo major upgrades. Two critical components of this Phase II upgrade are the High Granularity Timing Detector (HGTD) and the new all-silicon Inner Tracker (ITk) . These systems are designed to extend the detector’s spatial and temporal coverage, improve pile-up mitigation, and will significantly enhance sensitivity to rare and exotic signatures such as Long-Lived Particles.

2.3.1 High Granularity Timing Detector (HGTD)

The HGTD [5] will be installed in the forward region, covering the pseudorapidity range $2.4 < |\eta| < 4.0$, between the endcaps of the ITk and the LAr calorimeters, at $z = \pm 3.5$ m from the interaction point. It will consist of four active layers of Low-Gain Avalanche Detectors (LGADs), a technology capable of delivering a time resolution of approximately 30 ps per charged track, even after heavy irradiation.

The main purpose of the HGTD is to provide precise time-of-arrival measurements for particles traversing this forward region. This is essential to mitigate the effects of pile-up, where up to 200 simultaneous proton-proton interactions per bunch crossing are expected. The timing information allows for effective 4D vertex reconstruction by separating spatially overlapping interactions that occur at different times. In addition, such precision timing enables the identification of delayed decay products from LLPs, increasing the detector’s capabilities for BSM physics in regions that were previously difficult to access.

2.3.2 Inner Tracker (ITk)

The Inner Tracker (ITk) [6] will replace the current Inner Detector and extend tracking capabilities from $|\eta| < 2.5$ up to $|\eta| < 4.0$. It is entirely based on silicon technologies, consisting of a high-resolution Pixel Detector at the innermost radii and a Strip Detector in the outer regions. It consists entirely of silicon sensors, offering improved granularity and precision in vertex reconstruction. It is composed of a Pixel Detector and a Strip Detector arranged in both barrel and endcap geometries.

2.4 Observing Long-Lived Particles with ATLAS

Long-Lived Particles (LLPs) are detected in ATLAS through several distinctive signatures, such as displaced vertices and kinked tracks [7]. LLPs decay far from the primary vertex, leaving behind decay products that do not follow typical trajectories. Even if the detector was not originally designed to study them, it is still possible to use data from subsystems, such as the Inner Detector, which can be used to reconstruct the displaced vertices. Moreover, LLPs may produce kinked tracks where a particle's trajectory sharply bends, which can be traced back using ATLAS's algorithms. These are just two examples of the track types that can alert the presence of LLPs. An illustration of these and other track signatures that can be observed in LHC detectors is shown in Figure 2.2. Finally, the trigger system is designed to identify events with unusual signatures, such as those with missing energy, which may indicate the creation of a new particle.

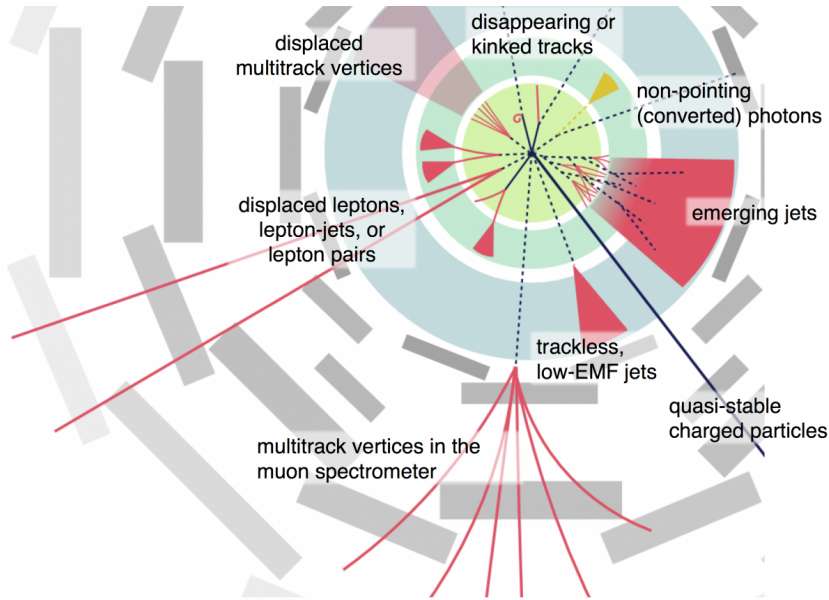


Figure 2.2: Schematic of atypical LLPs signatures in LHC detectors. [8]

However, particular challenges arise when searching for light LLPs, whose decay products tend to be soft and may carry too little energy to pass trigger thresholds or be reconstructed efficiently by standard algorithms. Their signatures can easily be confused with background, especially in high-pileup environments. In addition, their decays may occur within dense detector regions, making them harder to isolate or distinguish from hadronic activity. These factors significantly reduce the sensitivity of traditional searches. This report specifically focuses on studying such light LLP scenarios, aiming to evaluate the extent to which light LLPs may still be observed within the upgraded ATLAS detector.

Chapter 3

Monte Carlo Event Generation

3.1 Overview and objectives

Monte Carlo (MC) event generation plays a central role in high-energy physics, providing a bridge between theoretical models and experimental measurements. In this study, a full MC workflow is used to generate, process, and analyze simulated proton-proton collision events.

The chain begins with the definition of the theoretical model and Feynman rules, followed by event generation at the parton level using *MadGraph5_aMC@NLO* (MG5) [9]. These parton-level events are then passed to *PYTHIA 8* [10] for parton showering, hadronization, and particle decays, producing realistic event topologies. The resulting events are stored in standard formats such as HEPMC [11], which can be further analysed using *Rivet* [12], a framework for validating and comparing simulations to experimental analyses. Histograms and observables are then recorded in the YODA format [13].

This chapter outlines the full MC pipeline used in this study, from model definition to event generation. We discuss how different production mechanisms are handled, and how the relevant LLP properties, such as decay modes, are configured.

3.2 Monte Carlo algorithm

The Monte Carlo method [14] is a fundamental computational technique widely used in science for simulating complex stochastic processes, such as particle collisions. It enables the numerical evaluation of complex, high-dimensional integrals representing differential cross sections and phase space distributions that are otherwise analytically intractable.

In event generation, the goal is to simulate collision events according to the differential cross section $\frac{d\sigma}{d\Phi}$, where Φ denotes the multi-particle final-state phase space. The total cross section σ is obtained by integrating this differential cross section over all the allowed phase space configurations:

$$\sigma = \int \frac{d\sigma}{d\Phi} d\Phi \quad (3.1)$$

Direct evaluation of this integral is challenging due to the complicated structure of $\frac{d\sigma}{d\Phi}$, which often exhibits sharp peaks and singularities. These arise physically from processes where particles emit low-energy (soft) radiation or particles are emitted at very small angles relative to each other (collinear emissions), leading to enhanced probabilities in these kinematic regions.

Such features cause the integrand to vary rapidly, making traditional numerical integration inefficient or unstable. The MC approach addresses this by generating a large number of random events $\{\Phi_i\}$ distributed according to the normalized probability density :

$$P(\Phi) = \frac{1}{\sigma} \frac{d\sigma}{d\Phi} \quad (3.2)$$

Each event Φ_i corresponds to a specific kinematic configuration of outgoing particles, sampled according to $P(\Phi)$. An ensemble of N such events is generated, enabling the estimation of physical observables $\langle \mathcal{O} \rangle$ by averaging:

$$\langle \mathcal{O} \rangle \approx \frac{1}{N} \sum_{i=1}^N \mathcal{O}(\Phi_i) \quad (3.3)$$

Event weights can also be introduced to unweight or reweight events, optimizing computational efficiency and enabling systematic uncertainty evaluation. Generating events according to $P(\Phi)$ involves complex algorithms such as importance and rejection sampling. These techniques efficiently focus computational effort on the most relevant regions of the phase space where the differential cross section is large.

In general, the Monte Carlo algorithms [15] transform theoretical differential cross sections into realistic simulated event samples, which are essential to compare theoretical predictions with experimental data, optimize detector designs, and interpret results in collider experiments.

3.3 Rivet framework

Rivet¹ [12] is a widely used modular framework designed to analyze Monte Carlo (MC) simulated events and validate them against experimental measurements, primarily from LHC experiments. It provides a library of pre-implemented C++ analysis routines based on published results, but also allows users to develop customized analyses tailored to specific physics studies. Rivet works by reading events stored in the HEPMC format, which contains detailed information about particles and vertices in each simulated collision. Within Rivet, the analysis proceeds through three main phases as shown in Figure 3.1:

1. *init()*: projections are declared to select physics objects (e.g., final-state particles, jets), and histograms or other data containers are booked for output.
2. *analyze(...)*: each event is passed through the analysis where selection criteria are applied, and relevant observables are computed and filled into histograms.
3. *finalize()*: the accumulated histograms and statistics are normalized and then written to output files in the YODA format. YODA files are human-readable and compatible with plotting modules, allowing efficient comparison between different MC samples or against experimental data.

In this study, the analysis is mainly based on the *MC_JETS* routine. It uses the anti- k_T algorithm to reconstruct jets and applies basic selection criteria, which were extended to study displaced signatures relevant to long-lived particles.

¹Robust Independent Validation of Experiment and Theory.

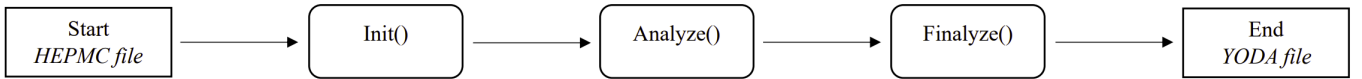


Figure 3.1: Execution flow of a Rivet routine.

3.4 Event generation with MG5

MG5 [9] is a powerful Monte Carlo event generator widely used in high-energy physics for simulating parton-level processes. Its primary purpose is to compute matrix elements at tree-level or next-to-leading order (NLO), enabling precise predictions for particle interactions. MG5 supports a variety of physics models and allows users to define specific production mechanisms, decay chains, and kinematic cuts with great flexibility.

In this study, MG5 is used to simulate processes involving LLPs within the framework of the Hidden Abelian Higgs Model. The specific model used, *HAHM-variableMW_v3_UFO* [16], extends the (SM) by introducing a hidden $U(1)_X$ gauge symmetry and an additional scalar field ϕ_H , which mixes with the SM Higgs boson after spontaneous symmetry breaking. This mixing results in two physical Higgs-like states: a SM-like Higgs h and a heavier scalar H , the latter capable of decaying into LLPs, modeled here as light scalars h_2 , which in turn decay into SM fermions. The model is implemented using *FeynRules* [17], a Mathematica package that derives interaction vertices directly from the Lagrangian and exports them in the Universal FeynRules Output (UFO) format compatible with MG5.

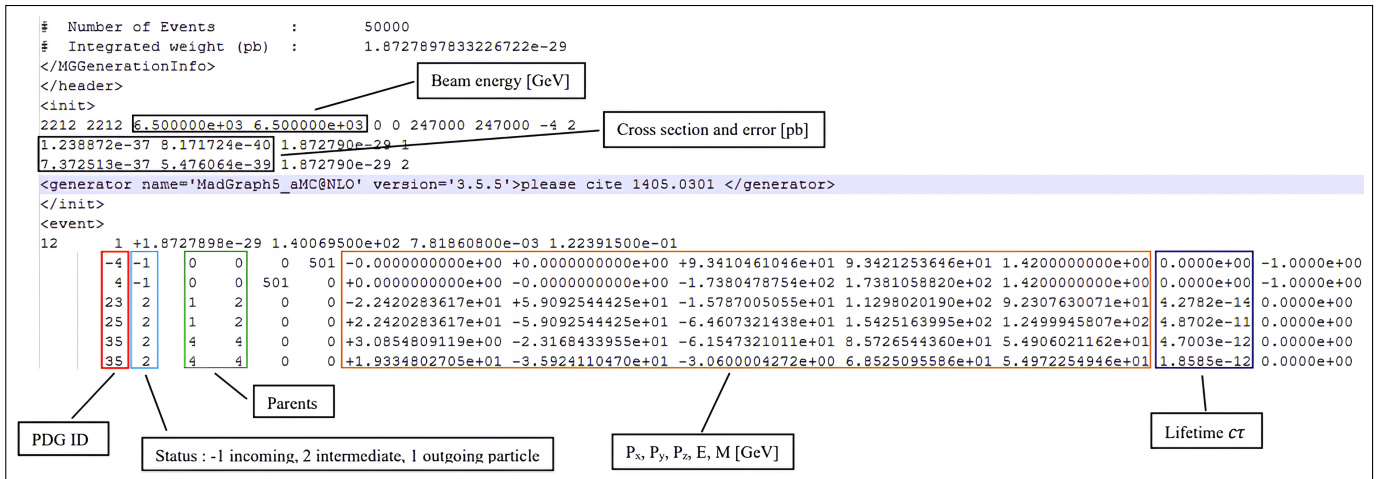


Figure 3.2: LHE file format.

We focused our study on three production mechanisms relevant for LLP searches: gluon fusion (ggh), vector boson fusion ($pp \rightarrow hjj$), and associated production with a vector boson ($pp \rightarrow Wh$ or $pp \rightarrow Zh$). These channels cover complementary kinematic regimes and allow us to probe different LLPs decay configurations in the detector. MG5 stores these unweighted events in the Les Houches Event (LHE) format [18], as shown in the figure 3.2. For simplicity, some loop-induced processes, such as gluon fusion via top-quark loops, are approximated by effective contact interactions. The process illustrated in Figure 3.3 represents this typical method. Here, the heavy Higgs decays into two LLPs h_2 , each decaying into fermion pairs. Although this introduces simplifications, it remains a standard and well-validated approach for phenomenological studies.

To efficiently produce a large number of event samples with varying parameters, a series of

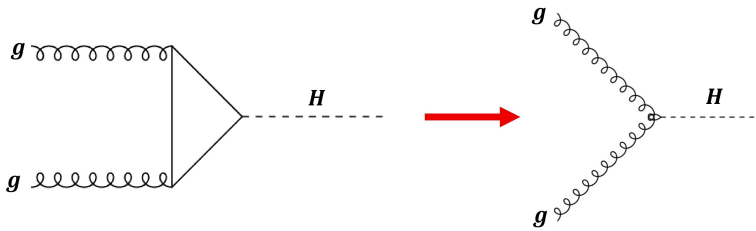


Figure 3.3: Example of Feynman diagram simplification, here for the ggH production mode.

```

import model sm
import model HAHM_variableMW_v3_UFO
define f = u c d s u~ c~ d~ s~ b b~ e+ e- mu+ mu- ta+ ta- t t~
define p = g u c d s u~ c~ d~ s~
define j = u c d s b u~ c~ d~ s~ b~
define vl = ve vm vt
define vl~ = ve~ vm~ vt~
define j~ = g u c d s u~ c~ d~ s~
define l+ = e+ mu+ ta+
define l- = e- mu- ta-
generate p p > w+ h, (w+ > l+ vl), (h > h2 h2, h2 > f f, h2 > f f)
add process p p > w- h, (w- > l- vl~), (h > h2 h2, h2 > f f, h2 > f f)
output script_ppWpmH_LLPMs_lepton_55
launch script_ppWpmH_LLPMs_lepton_55
shower=Pythia8
0
set nevents = 50000
set mhsinput 30
set mhinput 125
set epsilon 1e-10
set kap 1e-4
set time_of_flight 0
set event_norm = sum
set ebeam1 6800
set ebeam2 6800

```

Model import
Particle definitions
Defining the Production Processes
Start the parton showering and hadronization process
Simulation Parameters

Figure 3.4: Extract from a MG5 script used to generate events in the VH channel.

automated scripts were developed to handle the generation of events with MadGraph5 and their subsequent processing with PYTHIA8. An illustration of a basic script used for this workflow is shown in Figure 3.4. These scripts allow consistent control over global simulation parameters and ensure reproducibility across different configurations. Among the most relevant parameters are *nevents*, which sets the number of events to be generated, *ebeam*, which sets the energy of each proton beam (in GeV), here fixed at 6800 GeV to match the LHC Run 3 energy of $\sqrt{s} = 13.6$ TeV. The parameters *mhinput* and *mhsinput* correspond to the masses of the Standard Model Higgs boson and an additional heavy scalar.

3.5 Parton shower and hadronization with PYTHIA 8

Once the parton-level events are generated by MG5, they are passed to PYTHIA [10] which is designed to simulate high-energy particle collisions, particularly where quantum chromodynamics (QCD) effects dominate. It models the full evolution of collision events, starting from a few-body hard-scattering processes to multi-particle final states that detectors observe.

At the core of PYTHIA's simulation is the parton shower mechanism which models the evolution of high-energy colored partons (quarks and gluons) as they undergo successive branchings. This

process is described through a probabilistic algorithm which governs the evolution of parton distribution functions via collinear and soft gluon emissions. The shower evolves from the high-energy scale of a hard collision (set by the matrix element kinematics) down to a non-perturbative scale, effectively describing how jets of particles develop inside a detector.

Once the shower evolution reaches the non-perturbative scale (about 1 GeV), PYTHIA implements the hadronization stage, where colored partons are transformed into color-neutral hadrons, because quarks and gluons carry color charge and cannot exist as free particles due to color confinement. Instead, they are always bound together inside color-neutral hadrons.

In addition, PYTHIA simulates the decay of unstable particles, including the specific long-lived particles studied here. The decay channels are configurable, allowing the incorporation of BSM scenarios. This step ensures that the final event record contains realistic, stable particles compatible with detector signatures.

```

P 3 -4 0 0 9.3418757677912083e+01 9.3418757677912083e+01 0 21 0 0 -3 1 2 501
P 11 21 7.1094191983443284e+00 1.2627387986549053e+01 1.6877622174666470e+01 2.2245199459016401e+01 0 43 0 0 -12 2 1 501 2 504
V -2 0 0 0 0 0 1 0
P 4 4 0 0 -1.7381308417041208e+02 1.7381308417041208e+02 0 21 0 0 -3 1 1 501
V -3 0 0 0 0 0 2 0
P 5 23 -2.2420283616999999e+01 5.9092544425000000e+01 -1.5787005055000000e+01 1.1298020190289313e+02 9.2307630071000006e+01 22 0 0 -6 0
P 6 25 2.2420283616999999e+01 -5.9092544425000000e+01 -6.4607321438000000e+01 1.5425163994354830e+02 1.2499945807000000e+02 22 0 0 -7 0
V -4 0 0 0 0 0 2 0
P 7 -4 -1.7763568394002505e-15 -2.6645352591003757e-15 1.1475201528499063e+02 1.1475201528499063e+02 0 41 0 0 -1 1 2 504
P 17 4 5.4554997351735492e+00 -1.9652263087385389e+00 1.7011136711290884e+01 1.8034782061762353e+01 1.5000000000000000e+00 43 0 0 -18 1 1 505
V -5 0 0 0 0 0 1 0
P 8 4 1.7763568394002505e-15 3.5527136788005009e-15 -1.7381308417041211e+02 1.7381308417041211e+02 0 42 0 0 -2 1 1 501
V -6 0 0 0 0 0 1 0
P 9 23 -2.6118615712151847e+01 5.2523755475339392e+01 -1.0871588362605458e+01 1.0990822070620028e+02 9.2307630071000006e+01 44 0 0 -10 0

```

Figure 3.5: HEPMC file format.

The output of this full simulation stage is stored in the HEPMC file format, visible in Figure 3.5. Each event contains a list of vertices and particles, each with their associated properties [19]. For a particle entry **P**, available information includes the local ID, PDG ID, momentum components p_x , p_y , p_z , energy E , and mass M in GeV, as well as a status code. For a vertex entry **V**, the record includes the local vertex ID, space-time coordinates, the number of outgoing particles from that vertex and the status.

Chapter 4

Preliminary Studies of Long-Lived Particle Kinematics

4.1 Description of the simulated LLP scenarios

This chapter focuses on preliminary studies conducted to characterize the kinematic signatures of Long-Lived Particles, comparing them to the experimental detection capabilities of the ATLAS detector. Three main LLP production channels were initially considered:

Gluon-Gluon fusion (ggH):

This channel features the largest production cross section at the CM energy of $\sqrt{s} = 13.6$ TeV, with about 52.2 pb for a 125 GeV Higgs boson mass [20]. This is the main advantage of this mode and it ensures a large number of produced events, improving statistical sensitivity for LLP searches. Gluon fusion is the dominant production mechanism for scalar particles and serves as a baseline for signal generation. The corresponding Feynman diagram is shown in Figure 4.1.

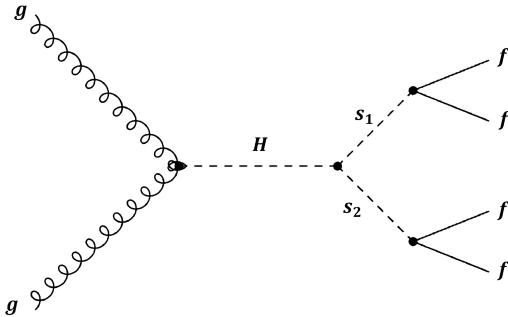


Figure 4.1: Feynman diagram for Higgs boson production via gluon-gluon fusion (ggH).

Associated production with Vector Bosons (VH):

In this process, LLPs are produced in association with W and Z bosons, with cross sections of approximately 1.46 pb for WH and 0.95 pb for ZH at 13.6 TeV. The presence of the vector boson provides a clean experimental signature, as its decay products can trigger the detector and help discriminate signal events from background. An illustration of this process is provided in Figure 4.2.

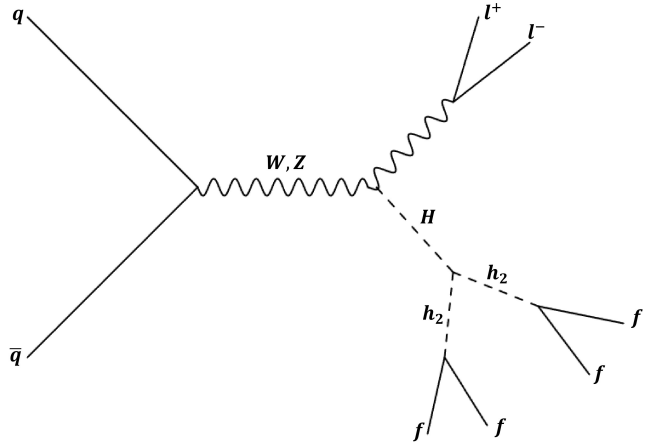


Figure 4.2: Feynman diagram for the associated production of a Higgs boson with a vector boson.

Vector Boson Fusion (VBF):

Although initially considered, this channel was not studied in detail due to time constraints. This mode is characterized by the exchange of vector bosons between incoming quarks, leading to the production of LLPs accompanied by two energetic jets in the forward regions of the detector. The cross section for VBF production at 13.6 TeV is approximately 4.1 pb. The Feynman diagram for this process is shown in Figure 4.3.

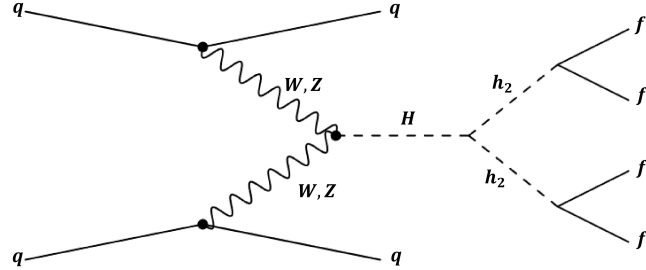


Figure 4.3: Representative Feynman diagram for Higgs boson production via Vector Boson Fusion.

The production channel associated with top quark pairs ($t\bar{t}H$) is not considered in this study due to its significantly smaller cross section at 13.6 TeV (approximately 0.57 pb) compared to the other channels. Including $t\bar{t}H$ would require more complex modeling and larger event samples to reach comparable sensitivity, which is beyond the scope of this current work.

Additionally, background processes were simulated to provide a realistic assessment of event selection performance. These background modes include: **Top quark pair production** ($pp \rightarrow t\bar{t}$), a common and significant source of jets and leptons. **Dijet production** ($pp \rightarrow jj$), representing QCD multijet events that constitute a large background due to their high cross section.

We have decided to explore several possible masses for the LLPs to cover a broad range of scenarios and assess the impact of mass variation on LLP detectability. The following plots will present results for all three LLP mass hypotheses considered in this study: 10 GeV, 30 GeV, and 55 GeV. Additional figures or alternative projections not shown here are available in the appendix. The typical LLP decays considered in this study involve a variety of fermionic final states, including light and heavy quarks as well as charged leptons.

4.2 Observables and kinematic distributions

In this section, we present an analysis of basic kinematic observables for the simulated LLPs. By analyzing distributions such as jet mass, transverse momentum, and pseudorapidity, we can assess the feasibility of detecting LLPs at the ATLAS detector and optimize selection criteria for future experiments. These distributions help identify characteristics that can be used to differentiate LLP signals from common background processes such as QCD events. We will also explore the impact of applying specific cuts to improve the signal-to-background ratio.

4.2.1 Jet mass and transverse momentum distributions

Firstly, we will analyze two kinematic observables: the jet mass and the transverse momentum (p_T) of the leading jet in LLP events, which can help distinguish LLP decays from background events.

Jet mass distribution:

We examine the distribution of the leading jet mass for the two LLP production modes: VH and ggH and compare them with the background process $pp \rightarrow jj$. The differential cross section $\frac{d\sigma}{dm(\text{jet 1})}$ [pb/GeV] is plotted as a function of the jet mass $m(\text{jet 1})$ [GeV]. By comparing the different hypotheses of the mass of LLP in the *jet-mass_1* histogram, we observe in Figure 4.4a that the expected mass peak is most pronounced for the lightest LLP, in both the ggH and VH production modes. In these cases, the peak stands out clearly and is well separated from the QCD background. However, this distinct structure becomes less visible for higher LLP masses. In Figure 4.4b, the VH channel still exhibits a noticeable peak, whereas the ggH channel appears almost flat, with no obvious structure around the expected mass. For the heaviest LLP mass of 55 GeV, shown in Figure 4.4c, the VH channel shows a steadily decreasing distribution without a local enhancement near the nominal mass. The ggH mode, on the other hand, presents a slight bump, but its significance is low and could easily be attributed to a statistical fluctuation.

We also observe notable peaks in the high-energy region between 80 and above 100 GeV, particularly in the VH production modes (ZH and WH). These features correspond to hadronic decays of the associated vector bosons, Z and W, whose invariant masses (91 GeV and 80 GeV, respectively) match the positions of the observed fluctuations. Since both bosons can decay to fermion pairs, the resulting jets can occasionally be reconstructed as the leading jet. In contrast, such peaks are absent in the ggH channel, where no vector boson is produced. As the LLP mass increases, these peaks fade due to phase space constraints and the lower boost of heavier LLPs, which reduces the probability of forming a single energetic jet. Additionally, detector resolution effects and the limited number of events in the high-mass regime contribute to smoothing out these distributions.

Transverse momentum distribution:

We now analyze the transverse momentum p_T distribution of the leading jet, shown as the differential cross section with respect to transverse momentum, expressed in [pb/GeV] as a function of p_T [GeV], using the histogram *jet_pT_1*. The transverse momentum is an important observable, as LLPs are typically produced in high-energy collisions that lead to high p_T values. By comparing the different LLP masses, we observe that the minimal transverse momentum of the signal decreases as the LLP mass increases. For an LLP mass of 10 GeV (Figure 4.5a), the ggH mode shows a distinct peak around 60 GeV, while the VH mode presents a broader

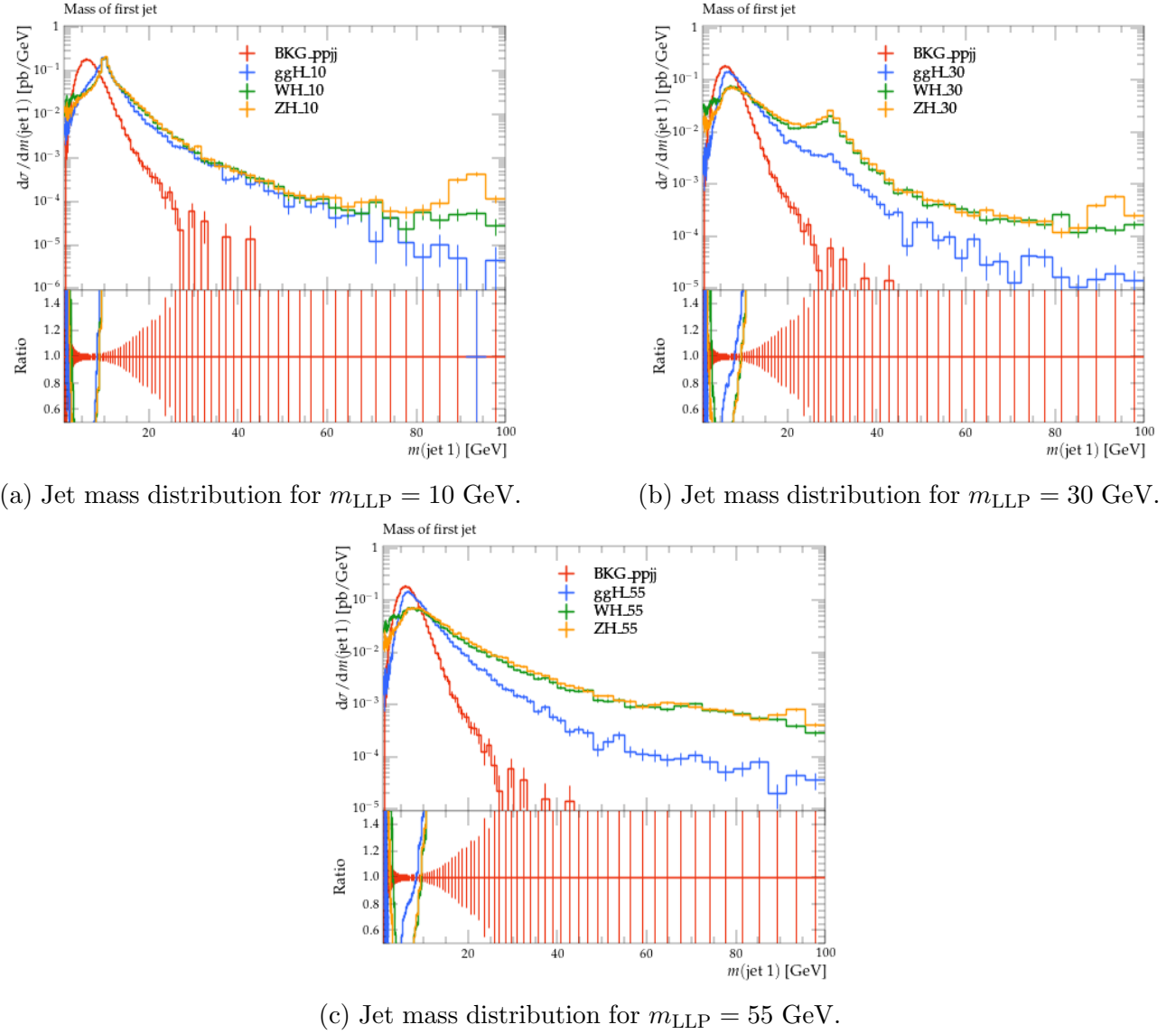


Figure 4.4: Comparison of leading jet mass distributions for the three LLP mass hypotheses.

distribution centered near 70 GeV. At 30 GeV (Figure 4.5b), both production channels display softened p_T spectra with less pronounced peaks. For the highest LLP mass, 55 GeV (Figure 4.5c), the ggH distribution reaches its maximum near 35 GeV, and the VH mode also exhibits lower transverse momentum values compared to the lighter mass scenarios.

These observations reflect the fact that heavier LLPs tend to be produced with lower boosts in the laboratory frame, particularly when their production is mediated by heavy intermediate states or occurs near the creation threshold. As a result, the visible decay products, such as the jets reconstructed from displaced decays, inherit lower transverse momenta. This effect is especially noticeable in the ggH channel, where the Higgs boson tends to be produced more centrally. Consequently, the higher the LLP mass, the more isotropic and softer the decay products become, leading to a downward shift in the p_T spectrum.

Beyond the purely technical analysis, the distributions discussed above offer physical insight into LLP production and decay mechanisms. The jet mass distribution reveals a resonant structure near the nominal LLP mass, particularly for lighter LLPs. This is a direct consequence of

4.2. Observables and kinematic distributions

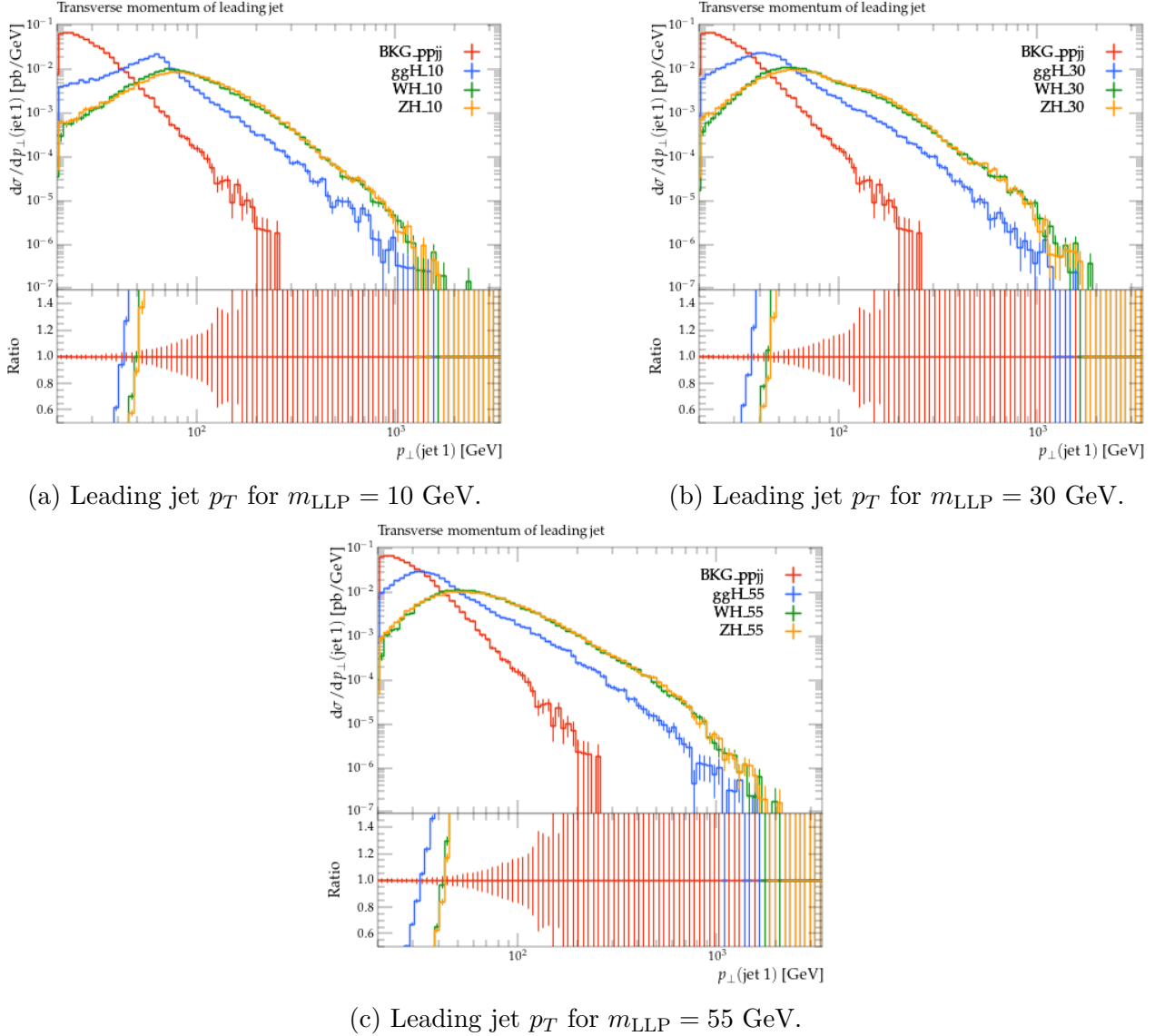


Figure 4.5: Comparison of leading jet transverse momentum distributions for the three LLP mass hypotheses.

the hadronic decay of the LLP into a confined set of particles that form a jet. Such a peak is not expected in QCD multijet background, where jets originate from standard parton fragmentation processes without such resonant behavior. This makes jet mass a useful discriminant for identifying low-mass LLP signals. The transverse momentum distribution further illustrates how LLP kinematics evolve with mass. Heavier LLPs are typically produced with lower boosts in the lab frame, and their decay products inherit less transverse momentum as a result. This explains the downward shift of the p_T spectrum observed for increasing LLP masses. In contrast, background QCD events predominantly populate the low- p_T region. Producing jets with high transverse momentum requires partons that carry a large fraction of the proton's momentum. However, such partons are rare, as described by the proton's parton distribution functions (PDFs). As a result, high- p_T QCD events are strongly suppressed.

4.2.2 Pseudorapidity distribution and detector acceptance

An important feature of the LLPs detection study is the pseudorapidity (η) distribution, which is particularly relevant to assess whether these processes, which produce LLPs, can be detected, in our case, by the ATLAS detector. The η distribution provides insights into the angular distribution of the LLPs and helps determine which events are within the detector acceptance.

The distribution of the leading jet displayed in Figure 4.6 is shown as the differential cross section, expressed in [pb] as a function of η . The acceptance of the ATLAS detector is defined by its ability to detect particles within specific pseudorapidity ranges, typically $|\eta| < 2.5$. This range corresponds to the central and barrel regions of the detector, where most particles are detected. The forward region is of particular interest, as some LLPs or their decay products may emerge at small angles with respect to the beam axis. It is important to note that the jets observed in this region may originate either from the decay of the LLP itself or from the initial interaction. This ambiguity demonstrates the need for careful analysis when interpreting forward-region activity.

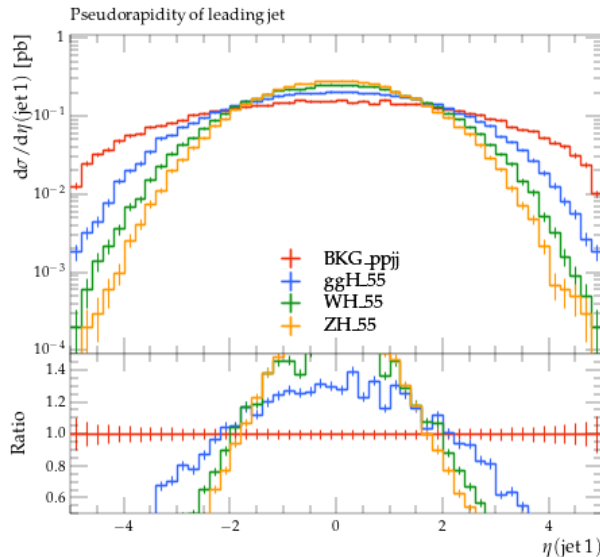


Figure 4.6: Pseudorapidity distribution of the leading jet for $m_{\text{LLP}} = 55 \text{ GeV}$.

As detailed in Chapter 2, the HGTD and ITK will play an important role here, as it will provide access to tracking in a region of the detector, specifically up to $|\eta| < 4.0$, starting from Phase-II of the LHC upgrade. Until now, tracking capabilities in ATLAS have been limited to the central region, which has been covered since Phase-I (Run 2 and Run 3) with the current Inner Detector. With the introduction of the HGTD and ITk in Phase-II, this acceptance will be significantly extended into the forward region, enabling more efficient reconstruction of displaced tracks and vertices in previously unexplored areas of the detector. By comparing η distributions for different LLP masses, no significant variation is observed. This reflects the fact that pseudorapidity is mainly used here as a proxy for detector geometry rather than a physically discriminating observable for LLP mass. In this sense, η is exploited to imitate the angular coverage of the ATLAS detector and to evaluate which signal regions fall within its acceptance. However, it must be noted that in some cases, LLPs may decay outside the geometrical acceptance of the detector or at such large distances from the interaction point that their decay products fall outside the sensitive detector volume. In such cases, the events become effectively invisible to the detector.

4.2.3 Role of cuts in improving signal detection

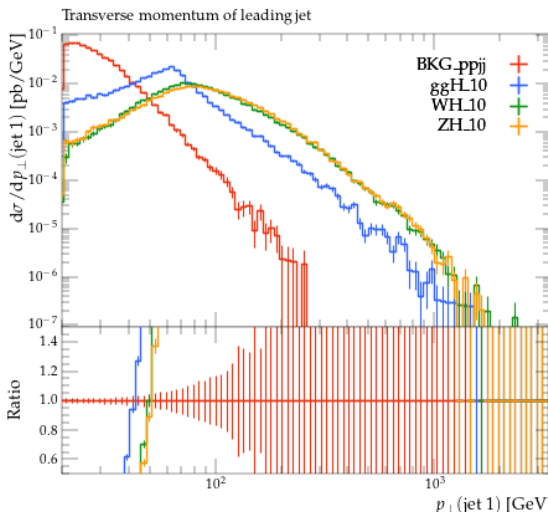
In high-energy physics, applying selection cuts is a standard method to enhance the visibility of rare signals by reducing contamination from dominant background processes. These cuts are typically part of a preselection phase, defined using simulated datasets in order to minimize the background while retaining as much signal as possible. Once optimized, these cuts are then applied to observed data in the final analysis. In the context of our work, which is a prospective study, we only rely on simulated samples. Therefore, the full workflow is based on Monte Carlo simulations as discussed earlier. Signal and background events are generated, relevant observables are analyzed to identify discriminating features, and cuts are defined accordingly. The goal is to anticipate which values or ranges of these observables might enhance the visibility of LLP decays and reduce the background. Here, we had time to focus on two cuts: the transverse momentum cut and the pseudorapidity cut.

In this context, the effectiveness of a specific cut can be quantitatively evaluated through its efficiency, defined as the ratio of the number of events that pass the cut to the total number of events before the cut. Mathematically, if N_{after} and N_{before} are the number of events after and before the cut respectively, the efficiency ε is given by:

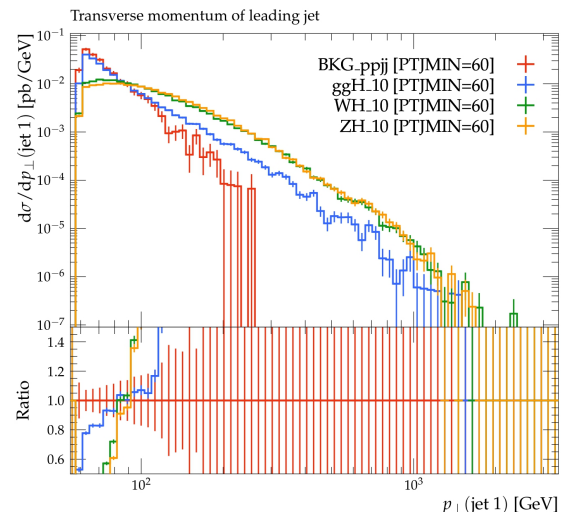
$$\varepsilon = \frac{N_{\text{after}}}{N_{\text{before}}}$$

Efficiencies are computed separately for signal and background samples, and can also be combined to determine the total efficiency after a series of cuts.

In Figure 4.7, we show the distribution of $p_T(\text{jet 1})$ before and after applying a threshold of $p_T > 60$ GeV. This value was chosen based on the separation observed between signal and background distributions, and the post-cut distribution confirms its effectiveness: a large portion of the low- p_T QCD background is eliminated, while the LLP signal remains mostly unaffected in the targeted production channels. Quantitatively, this cut retains approximately 61% of the total signal, while reducing the QCD background to only 7% of its initial state. Although a more stringent threshold could be applied, this selection already yields a notable improvement in signal-to-background ratio.



(a) Before applying the $p_T > 60$ GeV cut.



(b) After applying the $p_T > 60$ GeV cut.

Figure 4.7: Comparison of leading jet p_T distribution for $m_{\text{LLP}} = 10$ GeV before and after the cut.

Regarding the pseudorapidity, Figure 4.8 displays the $\eta(\text{jet 1})$ distribution before and after applying the forward-region condition $2.5 < |\eta| < 4.0$. Beyond background reduction, this cut has a clear experimental motivation: it directly targets the acceptance region covered by new forward instrumentation, such as the HGTD and extended ITk. Importantly, this step also allows us to study how the angular distribution of LLP decay products maps onto the upgraded detector geometry. From an efficiency standpoint, however, this selection has a relatively asymmetric effect on signal and background. This selection retains only about 16% of the total signal, while 26% of the QCD background passes the same cut. The main purpose of the $|\eta|$ cut is to significantly reduce the overwhelming QCD background, which dominates in the central region. However, the surviving events in this forward range are not discarded; they may well correspond to LLPs or their decay products. This selection thus acts as focusing filter, improving signal-to-background discrimination while preserving sensitivity to signal topologies compatible with the upgraded detector acceptance.

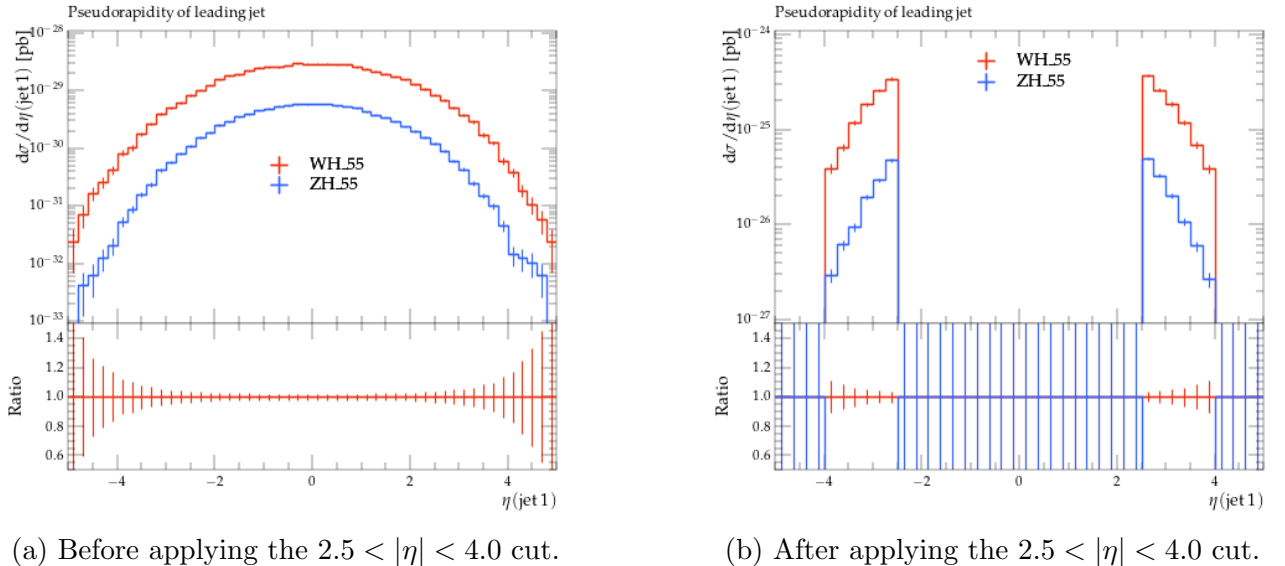


Figure 4.8: Comparison of leading jet η distribution for $m_{\text{LLP}} = 55$ GeV before and after the cut.

Conclusion

My work during this internship focused on assessing the observability of light Long-Lived Particles (LLPs) at the HL-LHC with the ATLAS detector. I began with a technical study of the event generation process using tools such as MadGraph5_aMC@NLO, Pythia, and Rivet and I implemented a full pipeline to simulate LLP production in several Higgs-associated channels. I then generated dedicated samples in the Hidden Abelian Higgs Model (HAHM), targeting low-mass LLPs, and performed a preliminary analysis on basic observables, assessing the impact of selection cuts and detector geometry.

As I continue my internship, I plan to extend this study by including the Vector Boson Fusion (VBF) production mode. Beyond this, several other directions could be explored to refine the analysis. These include incorporating displaced vertex observables, which are particularly relevant for LLP detection, as well as implementing a multivariate or machine learning based analysis to better refine signal regions.

Bibliography

- [1] G. Aad, T. Abajyan, Abbott, and A. Collaboration, “Observation of a new particle in the search for the standard model higgs boson with the atlas detector at the lhc,” *Physics Letters B*, vol. 716, no. 1, pp. 1–29, Sep. 2012, ISSN: 0370-2693. DOI: [10.1016/j.physletb.2012.08.020](https://doi.org/10.1016/j.physletb.2012.08.020). [Online]. Available: <http://dx.doi.org/10.1016/j.physletb.2012.08.020>.
- [2] N. Bakhet, M. Y. Khlopov, and T. Hussein, *Phenomenology of hidden abelian higgs model at hadron colliders using neural networks and monte carlo techniques (gauge sector Z_{HAHM} scalar sector h)*, 2015. arXiv: [1507.02594 \[hep-ph\]](https://arxiv.org/abs/1507.02594). [Online]. Available: <https://arxiv.org/abs/1507.02594>.
- [3] T. Chehab, L. D. Corpe, A. Goudelis, A. Haddad, and L. Millot, *Constraints on asymmetric production of long-lived scalars at the large hadron collider*, 2025. arXiv: [2502.18021 \[hep-ph\]](https://arxiv.org/abs/2502.18021). [Online]. Available: <https://arxiv.org/abs/2502.18021>.
- [4] R. M. Bianchi and A. Collaboration, “ATLAS experiment schematic or layout illustration,” General Photo, 2022. [Online]. Available: <https://cds.cern.ch/record/2837191>.
- [5] “Technical Design Report: A High-Granularity Timing Detector for the ATLAS Phase-II Upgrade,” CERN, Geneva, Tech. Rep., 2020. [Online]. Available: <https://cds.cern.ch/record/2719855>.
- [6] “Technical Design Report for the ATLAS Inner Tracker Pixel Detector,” CERN, Geneva, Tech. Rep., 2017. DOI: [10.17181/CERN.FOZZ.ZP3Q](https://doi.org/10.17181/CERN.FOZZ.ZP3Q). [Online]. Available: <https://cds.cern.ch/record/2285585>.
- [7] J. Alimena, J. Beacham, M. Borsato, H. Russell, *et al.*, “Searching for long-lived particles beyond the standard model at the large hadron collider,” *Journal of Physics G: Nuclear and Particle Physics*, vol. 47, no. 9, p. 090 501, Sep. 2020, ISSN: 1361-6471. DOI: [10.1088/1361-6471/ab4574](https://doi.org/10.1088/1361-6471/ab4574). [Online]. Available: <http://dx.doi.org/10.1088/1361-6471/ab4574>.
- [8] H. Russell, *An experimental introduction to longlived particle searches at the lhc*, Diapositives, 2017. [Online]. Available: https://indico.cern.ch/event/607314/contributions/2542309/attachments/1447873/2231444/20170424_LLPs.pdf.
- [9] J. Alwall, M. Herquet, F. Maltoni, O. Mattelaer, and T. Stelzer, “Madgraph 5: Going beyond,” *Journal of High Energy Physics*, vol. 2011, no. 6, Jun. 2011, ISSN: 1029-8479. DOI: [10.1007/jhep06\(2011\)128](https://doi.org/10.1007/jhep06(2011)128). [Online]. Available: [http://dx.doi.org/10.1007/JHEP06\(2011\)128](http://dx.doi.org/10.1007/JHEP06(2011)128).
- [10] Pythia Collaboration, *Pythia 8.3 online manual*, <https://pythia.org/manuals/pythia8313>Welcome.html>, The Pythia Group, 2023.
- [11] M. Dobbs and J. B. Hansen, “The HepMC C++ Monte Carlo event record for High Energy Physics,” *Comput. Phys. Commun.*, vol. 134, pp. 41–46, 2001. DOI: [10.1016/S0010-4655\(00\)00189-2](https://doi.org/10.1016/S0010-4655(00)00189-2). [Online]. Available: <https://cds.cern.ch/record/684090/files/soft-2000-001.pdf>.

- [12] C. Bierlich, A. Buckley, J. Butterworth, *et al.*, *Robust independent validation of experiment and theory: Rivet version 4 release note*, 2024. arXiv: 2404.15984 [hep-ph]. [Online]. Available: <https://arxiv.org/abs/2404.15984>.
- [13] A. Buckley, L. D. Corpe, M. Filipovich, *et al.*, “Consistent, multidimensional differential histogramming and summary statistics with yoda 2,” *SciPost Physics Codebases*, Jan. 2025, ISSN: 2949-804X. DOI: 10.21468/scipostphyscodeb.45. [Online]. Available: <http://dx.doi.org/10.21468/SciPostPhysCodeb.45>.
- [14] F. James, “Monte Carlo theory and practice,” *Rep. Prog. Phys.*, vol. 43, pp. 1145–1189, 1980. DOI: 10.1088/0034-4885/43/9/002. [Online]. Available: <https://cds.cern.ch/record/133919>.
- [15] A. Buckley, J. Butterworth, S. Gieseke, *et al.*, “General-purpose event generators for lhc physics,” *Physics Reports*, vol. 504, no. 5, pp. 145–233, Jul. 2011, ISSN: 0370-1573. DOI: 10.1016/j.physrep.2011.03.005. [Online]. Available: <http://dx.doi.org/10.1016/j.physrep.2011.03.005>.
- [16] A. CERN, *Madgraph model: Hahm_variablemw_v3_ufo*, <https://gitlab.cern.ch/tbold/athena/-/tree/2e8d28b7c2a4422ee94ed85f8bac1f43a20ba752/Generators/MadGraphModels/python/models>, 2025.
- [17] A. Alloul, N. D. Christensen, C. Degrande, C. Duhr, and B. Fuks, “FeynRules 2.0 — a complete toolbox for tree-level phenomenology,” *Computer Physics Communications*, vol. 185, no. 8, pp. 2250–2300, Aug. 2014, ISSN: 0010-4655. DOI: 10.1016/j.cpc.2014.04.012. [Online]. Available: <http://dx.doi.org/10.1016/j.cpc.2014.04.012>.
- [18] J. Alwall, A. Ballestrero, P. Bartalini, *et al.*, “A standard format for les houches event files,” *Computer Physics Communications*, vol. 176, no. 4, pp. 300–304, Feb. 2007, ISSN: 0010-4655. DOI: 10.1016/j.cpc.2006.11.010. [Online]. Available: <http://dx.doi.org/10.1016/j.cpc.2006.11.010>.
- [19] SMASH Collaboration, *Smash user guide: Hepmc output format*, https://theory.gsi.de/~smash/userguide/current/doxypage_output_hepmc.html, Accessed: 2025-05-25, 2024.
- [20] S. Navas *et al.*, “Review of particle physics,” *Phys. Rev. D*, vol. 110, no. 3, p. 030 001, 2024. DOI: 10.1103/PhysRevD.110.030001.

Appendices

Distributions of the three analyzed variables before and after the transverse momentum cut

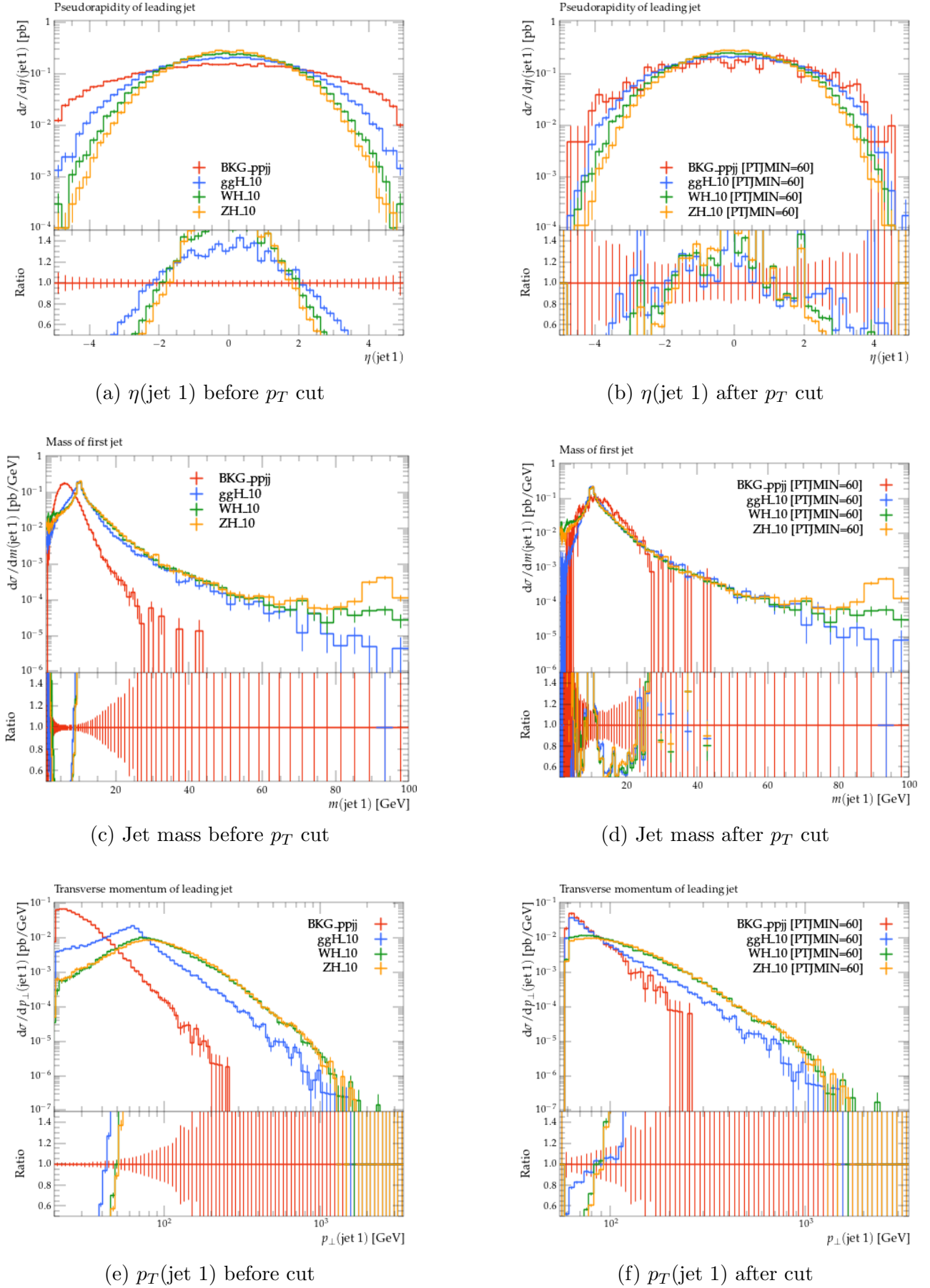
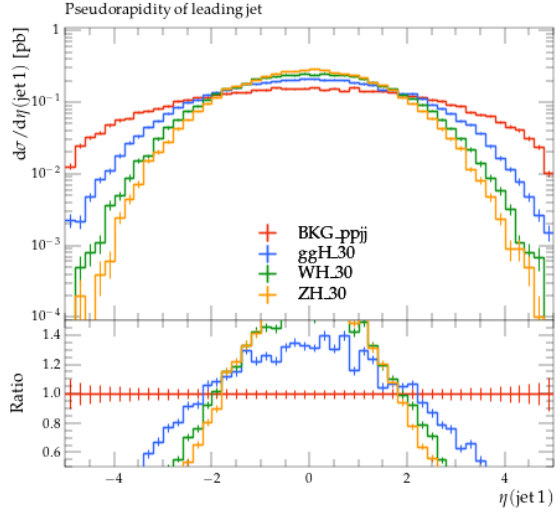
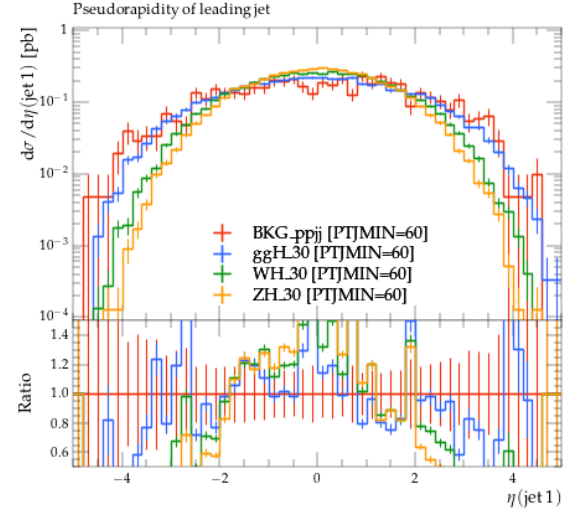


Figure 9: LLP mass = 10 GeV.

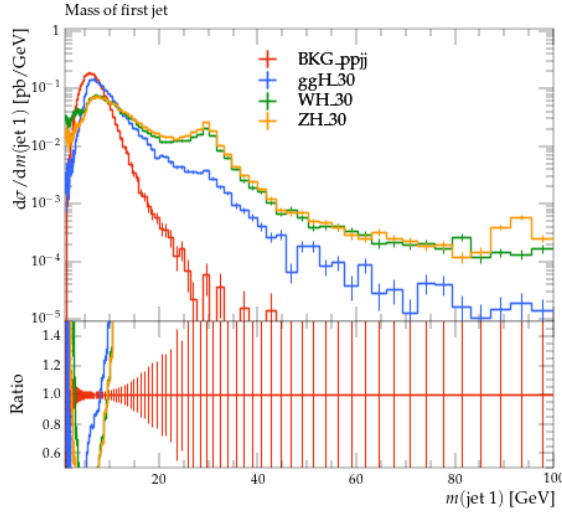
Bibliography



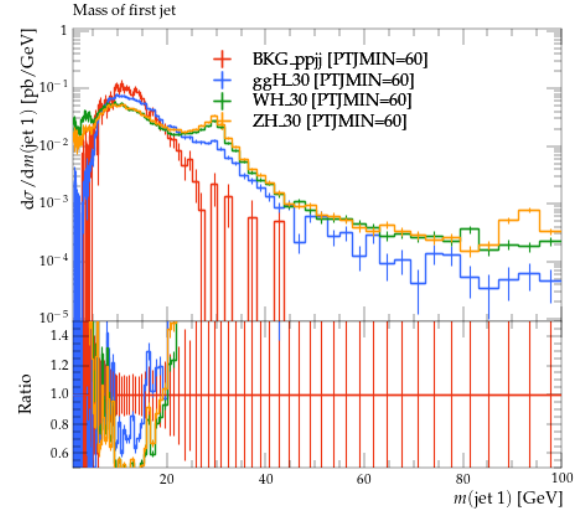
(a) $\eta(\text{jet 1})$ before p_T cut



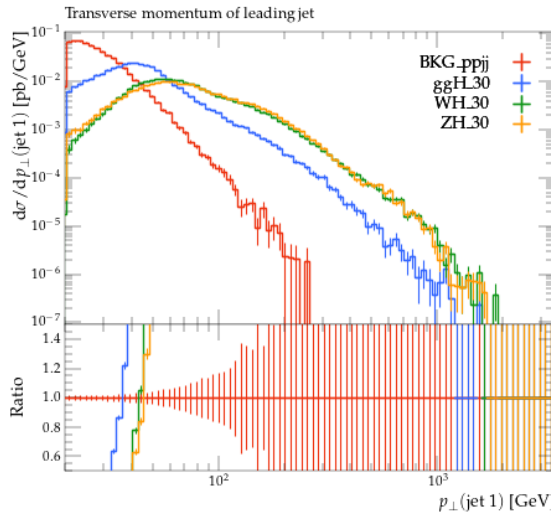
(b) $\eta(\text{jet 1})$ after p_T cut



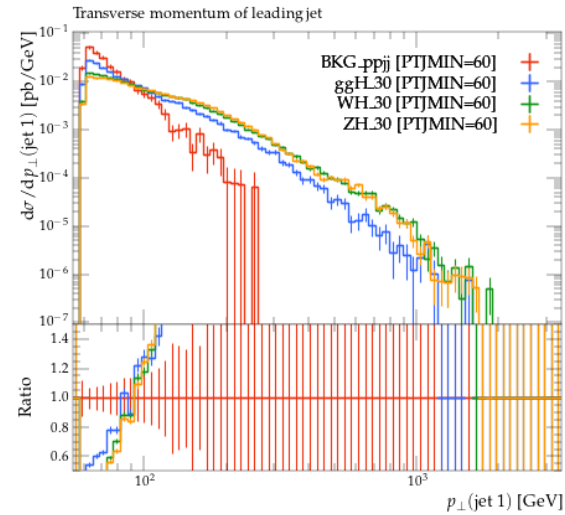
(c) Jet mass before p_T cut



(d) Jet mass after p_T cut



(e) $p_T(\text{jet 1})$ before cut



(f) $p_T(\text{jet 1})$ after cut

Figure 10: LLP mass = 30 GeV.

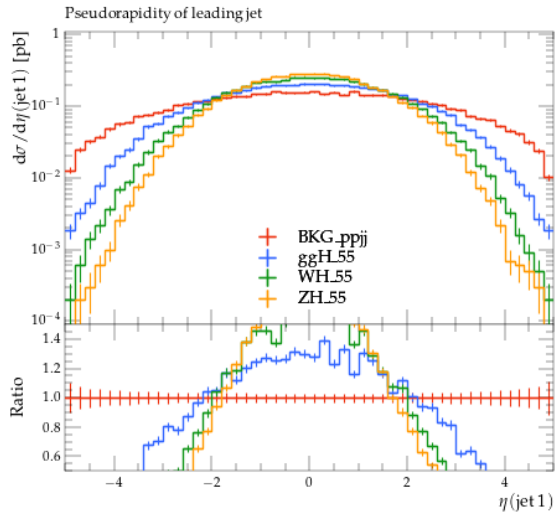
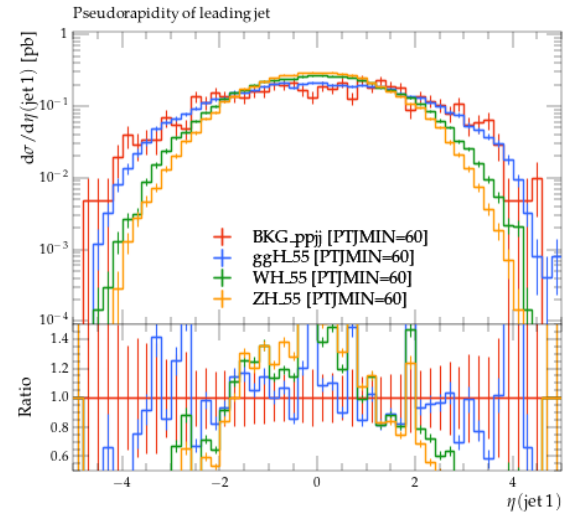
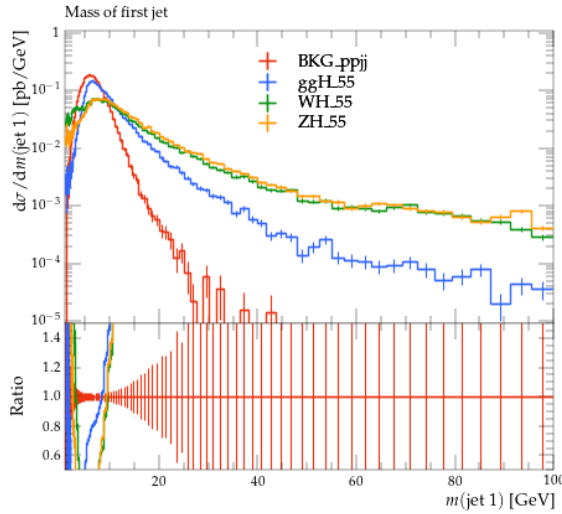
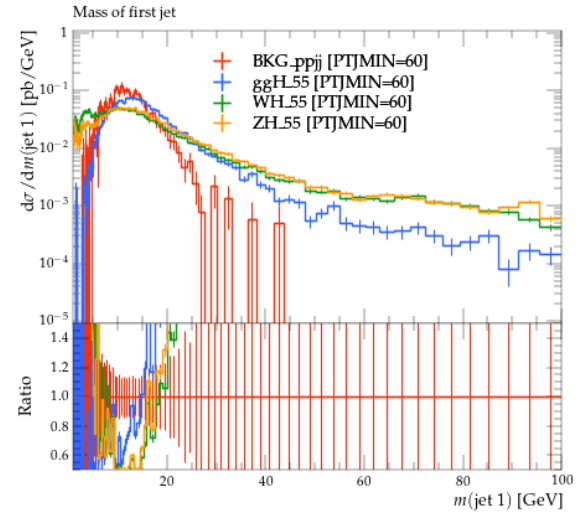
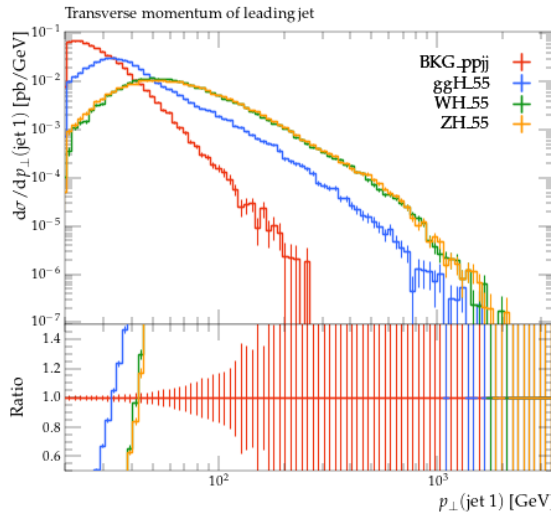
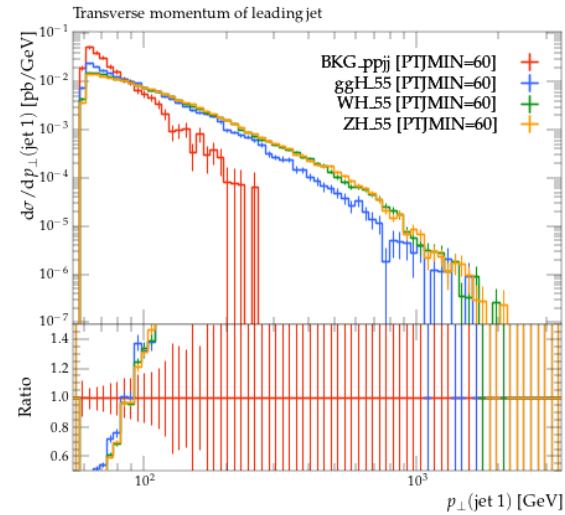
(a) $\eta(\text{jet 1})$ before p_T cut(b) $\eta(\text{jet 1})$ after p_T cut(c) Jet mass before p_T cut(d) Jet mass after p_T cut(e) $p_T(\text{jet 1})$ before cut(f) $p_T(\text{jet 1})$ after cut

Figure 11: LLP mass = 55 GeV.